Effect of iodine doping of phthalocyanine on the photocurrent generation in a phthalocyanine/C_{60} heterojunction

Shinsei Mizuta, Masatoshi Iyota, Senku Tanaka, Ichiro Hiromitsu*

Department of Material Science, Faculty of Science and Engineering, Shimane University, Matsue 690-8504, Japan

Abstract

Photocurrent generation in an indium-tin oxide (ITO)/iodine-doped Ni-phthalocyanine (NiPc-I_x)/C_{60}/In/Al heterojunction device with $x \sim 1$ was studied. By keeping the device in air after preparation, the device slowly reached a stationary state in which the sign of the photocurrent is opposite to that of a non-doped ITO/NiPc/C_{60}/In/Al device although the rectification direction for the dark current is the same. By a simulation of incident photon-to-current conversion efficiency spectra and a measurement of internal electric field by electroabsorption spectroscopy, it was elucidated that, in the doped device, the band bending near the phthalocyanine/C_{60} interface is absent and the photocurrent is generated by a weak Schottky barrier at the C_{60}/In interface. It is also shown that the C_{60} film encapsulates the doped iodine into the NiPc-I_x layer to stabilize the doping level and prevent the reaction of iodine with In.

Keywords: Organic device; Heterojunction; Doped organic semiconductor; Charge transfer complex; Electroabsorption

* Corresponding author: Tel.: +81 852 32 6391; fax: +81 852 32 6409
E-mail address: hiromitu@riko.shimane-u.ac.jp (I. Hiromitsu)

1. Introduction

Organic-semiconductor devices, e.g. solar cells, light emitting diodes, and transistors, are being extensively studied in these days. Much effort has been made to improve and control the device characteristics. One approach for this purpose is the doping of organic semiconductors, i.e. doping of a donor (acceptor) layer with electron acceptors (donors). The doping alters the conductivity and the Fermi level of the host materials, which significantly affects the device performances. Many results have been reported on the doping effects [1-13]. In the case of phthalocyanine(Pc)-based devices, tetrafluoro-tetracyano-quinodimethan (F_4-TCNQ) [2,3,5] and iodine [11,12] have been used as the dopants. The F_4-TCNQ doping can be achieved by co-evaporation of the host and the dopant molecules, which enables an easy control of the doping level. The range of the doping level of F_4-TCNQ ever studied is as wide as 0.1 ~ 30 mol%. The iodine doping, on the other hand, is achieved by a penetration of iodine gas into the host layer, so that the control and measurement of the doping level of iodine is relatively difficult. A more serious problem of the iodine doping is the reaction of the doped iodine with electrodes. Most electrode materials, e.g., Al, Au and In, easily react with iodine, so that the electrodes made of these materials are degraded. The degradation is especially serious when the doping level is high, so that the iodine-doped devices ever reported have low doping levels [10-12].

Apart from the device applications, however, the iodine-doped Pc's with high doping levels were extensively studied in 1970's-1980's [14-16]. In those studies, Pc was reacted with iodine to form a charge transfer (CT) complex Pc-I_x with the doping level $x \sim 1$. Such heavily doped Pc's usually have a tetragonal lattice [16], in contrast to a monoclinic or triclinic lattice of non-doped Pc's [17-19], and have conductivity several orders higher than that of non-doped Pc's [14,15]. A typical example is Ni-phthalocyanine(NiPc)-I_1 CT complex which has a high

conductivity of typically 1 S/cm [15]. In spite of these extensive studies, the iodine-doped Pc's with high doping levels have never been applied to electronic devices due to the problem of electrode degradation. This problem must be overcome in order to use the heavily doped Pc's to electronic devices.

In the present study, photocurrent generation and internal electric field of a heterojunction system made of NiPc-I_x with $x \sim 1$ and pristine C_{60} have been investigated. The objective of the present study is to elucidate the stability and electrical properties of the Pc-I_x/C_{60} heterojunction system. It will be shown that the C_{60} film deposited on the NiPc-I_x film effectively encapsulates the doped iodine into the Pc layer and prevents the degradation of the top electrode. It will also be shown that the direction of the photocurrent is inverted by the iodine doping of Pc. The inversion of the photocurrent will be explained by a flattening of the band bending near the Pc/C_{60} interface.

2. Experiment

2.1. Sample preparation

NiPc was purchased from Kanto Chem. Co. and used after subliming twice in vacuum. C_{60} was purchased from Materials and Electrochemical Research Corp. and used after single sublimation in vacuum. An indium-tin oxide(ITO) substrate of 30 Ω/sq. sheet resistance was purchased from Geomatec.

The arrangement of the thin films in the ITO/NiPc-I_x/C_{60}/In/Al heterojunction system is shown in Fig. 1. The Al film is the supporting electrode for In because of a low conductivity of the In film. All the films except ITO were prepared by vacuum deposition under a pressure of 1×10^{-4} Pa. The procedure of the sample preparation was as follows. First, a NiPc film was deposited on the ITO substrate. Then, the NiPc film was doped with iodine by keeping the NiPc

film with iodine powder in a vacuum-sealed glass tube at 30°C for 2 days. It is known that this doping condition gives a doping level of the order of $x \sim 1$ for NiPc-I_x [20,21]. After the doping, thin films of C_{60}, In and Al were deposited on the NiPc-I_x film. The film-thicknesses were 150 nm for NiPc, 100 nm for C_{60}, 20 nm for In and 30 nm for Al. The speeds of the evaporation were 0.1 nm/s for NiPc and C_{60}, 0.02 nm/s for In and 0.05 nm/s for Al. The film thickness was monitored using a quartz oscillator (ULVAC CRTM-5000 or CRTM-6000) during the deposition. The effective area of the device was 0.3 cm^2.

2.2. Measurements

The IPCE (incident photon-to-current conversion efficiency) spectra were measured using a 300 W Xe lamp followed by a monochromator with the sample kept in He gas. The positive directions of the current and applied bias voltage (V_{bias}) are defined in Fig. 1. The current was measured from the voltage drop across a small resistance r. The internal electric field of the device was studied by electroabsorption (EA) spectroscopy in which an electric-field modulation $E_m \sin \omega_m t$ was applied to the device and a synchronous change in the transmitted light intensity ΔT was detected [22-24]. ΔT with the fundamental frequency ω_m has the following relationship with the static internal electric field E_0 in the device [22],

$$-\frac{\Delta T}{T} \propto \mathrm{Im}\chi^{(3)} E_0 E_m \sin \omega_m t \ , \qquad (1)$$

where T is the transmitted light intensity, and $\mathrm{Im}\chi^{(3)}$ is the imaginary part of the third-order electric susceptibility. Therefore, information about the internal electric field can be obtained by measuring $-\Delta T/T$ using a lock-in amplifier. In the EA measurement, the sample was kept in air. The work function of NiPc-I_x in air was measured on a photoemission-yield spectrometer (Riken Keiki, AC-2).

3. Results

3.1. Optical absorption

Figure 2(a) shows the optical absorption spectra of NiPc-I_x and NiPc films on quartz. The *Q* band of non-doped NiPc at 530-750 nm has a doublet structure because of a low crystal symmetry, but that of doped NiPc-I_x has a singlet structure because of a higher tetragonal symmetry [16]. NiPc-I_x shows another broad peak at 505 nm which is attributed to I_3^- [16,25]. Figure 2(a) also shows the spectrum after keeping the doped film for 9 months in air. It is observed that this spectrum is nearly identical with that of the non-doped NiPc film. This indicates that the doped iodine is slowly removed from the NiPc-I_x film.

Figure 2(b) shows the absorption spectra of the C_{60} films on quartz before and after treatment with iodine vapor by the procedure similar to that for the NiPc-I_x preparation. No substantial difference is observed between the two spectra of C_{60}, indicating that no reaction takes place between C_{60} and iodine. It is also noted that ITO does not react with iodine, because the absorption spectrum of ITO in the near IR region (800 nm < λ < 3000 nm, not shown here), which is sensitive to the electronic state of ITO, does not show any change by the treatment with iodine vapor.

Figure 2(c) shows the optical absorption spectra of NiPc-I_x/C_{60} and NiPc/C_{60} films on quartz. It is observed that the spectra of the NiPc-I_x/C_{60} films immediately after the preparation and after being kept in air for 9 months are identical. This indicates that no removal of the doped iodine occurs when the NiPc-I_x film is covered with a C_{60} film. Thus, the C_{60} film effectively encapsulates the iodine into the NiPc-I_x film. This makes the present device ITO/NiPc-I_x/C_{60}/In/Al stable, because, if the iodine reaches the In film through the C_{60} layer, it easily reacts with In and the In/Al electrode is degraded.

3.2. IPCE spectra

3.2.1. Experimental spectra

Figure 3 shows the IPCE spectra of the doped device ITO/NiPc-I_x/C_{60}/In/Al. The measurement was performed for two illumination directions, i.e. from the ITO and Al sides. The sign of the photocurrent showed an interesting aging effect. Immediately after the device preparation (Fig. 3(a)), negative photocurrent was observed for both illumination directions. The absolute value of IPCE is much smaller for the illumination from Al, because the transmission of the incident light through the In/Al electrode is very small. After aging for 33 days in air (Fig. 3(b)), the sign of the photocurrent with the illumination from Al became positive, while the sign with the illumination from ITO remained negative although the absolute value of IPCE was significantly reduced by the aging. After aging for 55 days (Fig. 3(c)), the sign of the photocurrent became positive for both illumination directions, which is a stationary state because nearly identical IPCE spectra were observed after aging for 118 days (Fig. 3(d)).

Figure 4 shows the IPCE spectra of non-doped device ITO/NiPc/C_{60}/In/Al. In contrast to the case of the doped device, the sign of the photocurrent was always negative even after aging for 118 days in air. The absolute value of IPCE was gradually reduced by the aging, and became 1/10 of the original value after 118 days, which is attributed to a degradation of the device.

3.2.2. Model for the simulation of IPCE spectra

In the IPCE spectra of the doped device in Fig. 3, the photocurrent at 550 nm < λ < 750 nm is small although NiPc-I_x has a strong absorption in this wavelength region. This indicates that the contribution of the NiPc-I_x excitation to the photocurrent generation is small. Then, the relatively large photocurrent observed at λ < 550 nm is generated mainly by the C_{60} excitation. In the IPCE spectra after aging for 33 days (Fig. 3(b)), the sign of the photocurrent at λ < 550

nm depended on the illumination direction. This indicates that there exist two photocurrent-active regions in the C_{60} layer near the NiPc-I_x/C_{60} and C_{60}/In interfaces. A similar situation has been reported for a Ga-doped ZnO/Zn-phthalocyanine/Cu Schottky-barrier cell [26].

Figure 5 shows a model that explains the present IPCE spectra in Fig. 3. In this model, photocurrent is generated by optical excitation in three regions. Region I is in the NiPc-I_x layer near the NiPc-I_x/C_{60} interface. Regions II and III, on the other hand, are in the C_{60} layer. Region II is near the NiPc-I_x/C_{60} interface, and region III is near the C_{60}/In interface. It is assumed that the sign of the photocurrent generated in regions I and II are negative, and that in region III is positive. Since the contribution of the NiPc-I_x excitation to the photocurrent generation is very small, the activity of region I is much smaller than that of region II and/or region III. When region II is more active than region III, negative photocurrent is observed for both illumination directions from ITO and Al, as observed in Fig. 3(a). When region III is more active than region II, positive photocurrent is observed as in Figs. 3(c) and (d). When the activities of regions II and III are comparable, the sign of the photocurrent depends on the illumination direction as observed in Fig. 3(b), i.e. negative for the illumination from ITO and positive from Al.

Using the model shown in Fig. 5, theoretical IPCE spectra were calculated by the following procedure. When the device is illuminated from ITO, the proportion of incident photons absorbed by region I is

$$P_{\mathrm{I}} = T_{\mathrm{ITO}} \exp[-\alpha_1(L_1 - d_{\mathrm{I}})] \times [1 - \exp(-\alpha_1 d_{\mathrm{I}})], \qquad (2)$$

where T_{ITO} is the transmissivity of the ITO film, α_1 is the optical absorption coefficient of the NiPc-I_x layer, which can be calculated from the optical absorption spectrum in Fig. 2(a), L_1 is the film thickness of NiPc-I_x, and d_{I} is the thickness of region I. Similarly, the proportions of the incident photons absorbed by the active regions II and III are

$$P_{II} = T_{ITO} \exp[-\alpha_1 L_1] \times [1- \exp(-\alpha_2 d_{II})], \quad (3)$$

$$P_{III} = T_{ITO} \exp[-\alpha_1 L_1] \times \exp[-\alpha_2 (L_2 - d_{III})] \times [1- \exp(-\alpha_2 d_{III})], \quad (4)$$

where α_2 is the optical absorption coefficient of the C_{60} layer, d_{II} and d_{III} are the thicknesses of regions II and III, respectively, and L_2 is the film thickness of C_{60}. IPCE is calculated by

$$\text{IPCE} = - \Phi_I \times P_I - \Phi_{II} \times P_{II} + \Phi_{III} \times P_{III}, \quad (5)$$

where Φ_I, Φ_{II}, and Φ_{III} are the quantum efficiencies for photocurrent generation in regions I, II, and III. In the present calculation, it was assumed that Φ_I is independent of the excitation wavelength, because the quantum efficiency of Pc has been reported to be wavelength independent [27]. On the other hand, it has been reported that the quantum efficiency of C_{60} increases at $\lambda \leq 500$ nm [28]. In the present calculation, it was assumed that Φ_{II} and Φ_{III} are expressed by the following formula.

$$\Phi_{II(\text{or III})} = \Phi^{(0)}_{II(\text{or III})} \times [1 + a \times (E - b)^2] \quad \text{for} \quad E \geq b, \quad (6)$$

$$\Phi_{II(\text{or III})} = \Phi^{(0)}_{II(\text{or III})} \quad \text{for} \quad E < b, \quad (7)$$

where $\Phi^{(0)}_{II}$ and $\Phi^{(0)}_{III}$ are the quantum efficiencies in the low energy limit of regions II and III, respectively, a and b are constants, and E is the photon energy in eV. In the present calculation, the values of a and b were fixed to 9 eV^{-2} and 2.7 eV, respectively, because these values gave a reasonable agreement between the experiment and calculation.

When illuminated from Al, P_I, P_{II} and P_{III} become as follows:

$$P_I = T_{Al}\, T_{In} \exp[-\alpha_2 L_2] \times [1- \exp(-\alpha_1 d_I)], \quad (8)$$

$$P_{II} = T_{Al}\, T_{In} \exp[-\alpha_2 (L_2 - d_{II})] \times [1- \exp(-\alpha_2 d_{II})], \quad (9)$$

$$P_{III} = T_{Al}\, T_{In} \times [1- \exp(-\alpha_2 d_{III})], \quad (10)$$

where T_{Al} and T_{In} are the transmissivities of the Al and In films, respectively.

3.2.3. Results of the simulation of IPCE spectra

Using the model shown in section 3.2.2, theoretical IPCE spectra were calculated and are shown in Fig. 3. In the calculation, it was found that the spectral line shape was insensitive to the values of the thicknesses d_{I}, d_{II} and d_{III} of the three active regions, so that these values were fixed to 20 nm. The agreement between the experimental and calculated IPCE spectra is satisfactory, as observed in Fig. 3. The estimated values of the quantum efficiencies Φ_{I}, $\Phi_{\mathrm{II}}^{(0)}$ and $\Phi_{\mathrm{III}}^{(0)}$ are shown in Table I, where $\Phi_{\mathrm{II}}^{(0)}$ and $\Phi_{\mathrm{III}}^{(0)}$ are the quantum efficiencies in the low energy limit as defined in Eqs. (6) and (7). Since the values of d_{I}, d_{II} and d_{III} were fixed in the present simulation, the estimated values of Φ_{I}, $\Phi_{\mathrm{II}}^{(0)}$ and $\Phi_{\mathrm{III}}^{(0)}$ virtually include information on d_{I}, d_{II} and d_{III} and can be interpreted as the carrier-generation activities of regions I, II and III. For ITO/NiPc-I_x/C_{60}/In/Al in Table I, Φ_{I} is much smaller than $\Phi_{\mathrm{II}}^{(0)}$ and $\Phi_{\mathrm{III}}^{(0)}$ in all the four cases. This indicates that the carrier-generation activity of NiPc-I_x is much smaller than that of C_{60}. In the as-prepared device, $\Phi_{\mathrm{II}}^{(0)}$ is larger than $\Phi_{\mathrm{III}}^{(0)}$. This indicates that region II controls the photocurrent generation, so that negative photocurrent was observed. After aging the device for 33 days, $\Phi_{\mathrm{II}}^{(0)}$ decreased significantly. As a result, $\Phi_{\mathrm{II}}^{(0)}$ and $\Phi_{\mathrm{III}}^{(0)}$ became in the same order. After aging for 55 days, $\Phi_{\mathrm{II}}^{(0)}$ decreased further, and $\Phi_{\mathrm{III}}^{(0)}$ became much larger than $\Phi_{\mathrm{II}}^{(0)}$. As a result, the sign of the photocurrent became positive. By a further aging up to at least 118 days, the values of $\Phi_{\mathrm{II}}^{(0)}$ and $\Phi_{\mathrm{III}}^{(0)}$ did not change. Thus, the device reached a stationary state after 55 days. This stationary state is considered to be the intrinsic state of ITO/NiPc-I_x/C_{60}/In/Al, in which the carrier-generation activity of region II is negligibly small and region III controls the photocurrent generation. The finite activity of region III indicates an

existence of a Schottky barrier at the C_{60}/In interface.

A similar simulation has been performed for the IPCE spectra of the non-doped device ITO/NiPc/C_{60}/In/Al by replacing α_1 in Eqs. (2)-(4) and (8) by the absorption coefficient of non-doped NiPc. Figure 4 shows the results of the simulation, and again the agreement between the experimental and calculated IPCE spectra is satisfactory. The estimated values of Φ_I, $\Phi_{II}^{(0)}$ and $\Phi_{III}^{(0)}$ are listed in Table I. It is observed that $\Phi_{III}^{(0)}$ is small but finite. This indicates that a small Schottky barrier exists at the C_{60}/In interface even in the non-doped device, which is so small that it has never been detected [29,30]. By the aging of the non-doped device, Φ_I, $\Phi_{II}^{(0)}$ and $\Phi_{III}^{(0)}$ decreased significantly, which is attributed to a degradation of the device.

3.3. Dark J-V curves

Figure 6 shows the dependence of the dark current density(J_{dark}) on V_{bias} for the non-doped ITO/NiPc/C_{60}/In/Al and the doped ITO/NiPc-I_x/C_{60}/In/Al. Both devices show clear rectification property with the same rectification direction. For the non-doped device, $|J_{dark}|$ decreased by the aging, which is attributed to the degradation of the device in agreement with the results in Fig. 4. The *J-V* curve of the doped device showed a significant aging effect. For $0 \leq V_{bias} \leq 1$ V, J_{dark} of the aged device is much smaller than that of the as-prepared device. This is explained by an increase of the barrier height for electron transport at the NiPc-I_x/C_{60} interface, as will be discussed in section 4.1.

3.4. Electroabsorption spectra

3.4.1. Schottky-junction devices with no doping

An EA measurement provides information about the internal electric field of organic devices.

We first show the EA spectra of non-doped Schottky-junction devices ITO/NiPc/In/Al and ITO/C_{60}/In/Al in order to study the lineshapes of the EA spectra of non-doped NiPc and C_{60} films. Figure 7 shows the EA spectra of ITO/NiPc/In/Al with V_{bias} = 1.5, 0, and −1.5 V. Generally, an EA spectrum of organic film is made by an overlap of the spectra coming from the bulk and interface of the film [23]. The intensity of the interface spectrum usually shows a very weak dependence on V_{bias} while that of the bulk shows strong dependence. Comparing the spectra for V_{bias} = 1.5 and −1.5 V in Figs. 7(a) and (c), the lineshapes are nearly the same although the signs of the EA signals are opposite to each other. This indicates that these spectra are made mainly by the bulk spectrum. The spectrum for V_{bias} = 0 V, on the other hand, has a line shape substantially distorted from the spectra for V_{bias} =1.5 and −1.5 V. This indicates that the intensity of the interface signal is in the same order with that of the bulk signal. The line shape of the bulk spectrum of NiPc film was obtained by a subtraction of the V_{bias} = −1.5 V spectrum from the V_{bias} = 1.5 V spectrum, assuming that the intensity of the interface signal is independent of V_{bias}. The interface spectrum, on the other hand, was obtained by subtracting the bulk spectrum from the V_{bias} = 0 V spectrum, where the intensity of the bulk spectrum for the subtraction was determined so as to obtain an interface spectrum having no sharp peak at 705 nm, on the assumption that this peak is attributed only to the bulk spectrum. The obtained bulk and interface spectra for V_{bias} = 0 V are shown in Fig. 7(b). The validity of the obtained interface spectrum was tested by checking whether the EA spectra for V_{bias} = 1.5 and −1.5 V were explained by the sum of the estimated bulk and interface spectra. The results are shown in Figs. 7(a) and (c). It is observed that the experimental spectra are very well explained by the sum spectra. Thus, the bulk and interface spectra of the non-doped NiPc film in the ITO/NiPc/In/Al Schottky-junction device have been obtained.

Figure 8 shows the EA spectra of ITO/C_{60}/In/Al for V_{bias} = 1, 0, and −1 V. By a similar

procedure to that for ITO/NiPc/In/Al, the bulk and interface spectra of the C_{60} film were obtained: The bulk spectrum was obtained by a subtraction of the V_{bias} = –1 V spectrum from the V_{bias} = 1 V spectrum, and the interface spectrum was obtained by a subtraction of the bulk spectrum from the V_{bias} = 0 V spectrum, where the intensity of the bulk spectrum for the subtraction was determined so as to obtain an interface spectrum having no peak at 550 nm. With the obtained bulk and interface spectra, the EA spectra for V_{bias} = 1 and –1 V, as well as the spectrum for V_{bias} = 0 V, were well explained as shown in Figs. 8(a) and (c).

3.4.2. Heterojunction device with no doping

Figure 9(a) shows the EA spectrum of the non-doped heterojunction device ITO/NiPc/C_{60}/In/Al with V_{bias} = 0 V. The signal at $\lambda \leq 570$ nm is attributed to C_{60}. The line shape is nearly identical with that of the bulk spectrum of C_{60} as shown in Fig. 9(a). The sign of the C_{60} signal is the same with that of the bulk signal in Fig. 8(b). This indicates that the electric field in the bulk of the C_{60} film in the heterojunction device has the same direction with that in the Schottky-junction device. The signal at $\lambda \geq 600$ nm, on the other hand, is attributed to NiPc. The line shape is identical with that of the bulk spectrum of NiPc as shown in Fig. 9(a). However, the sign of the NiPc signal is inverted from that of the bulk spectrum in Fig. 7(b). This indicates that the electric field in the bulk of the NiPc film in the heterojunction device has an opposite direction from that in the Schottky-junction device. The inversion of the electric field may be explained by a formation of a Schottky barrier at the ITO/NiPc interface, as will be discussed in section 4.1. Comparing the signal intensities of NiPc and C_{60} in Fig. 9(a), NiPc has much smaller intensity. This indicates that the average electric field in the NiPc layer is much smaller than that in the C_{60} layer by the following reason. The EA signal intensity is proportional to $\mathrm{Im}\chi^{(3)} E_0$ as shown in Eq. (1). The values of $\mathrm{Im}\chi^{(3)}$ for NiPc and C_{60} should be in

the same order, because the intensities of the bulk spectra in Figs. 7(b) and 8(b) are in the same order. Thus, the much smaller EA-signal intensity of NiPc in Fig. 9(a) is attributed to a much smaller internal electric field E_0 in the NiPc layer.

3.4.3. Heterojunction device with doping

Figure 9(b) shows the EA spectrum of the doped heterojunction device ITO/NiPc-I_x/C_{60}/In/Al immediately after the device preparation. It is observed that the line shape at $\lambda \leq 570$ nm is identical with that of the bulk spectrum of C_{60}, the sign of which is the same with that of the non-doped heterojunction device in Fig. 9(a). However, the intensity of the C_{60} spectrum became significantly smaller by the iodine doping of the NiPc layer. This indicates that the electric field in the C_{60} layer is significantly reduced by the doping although the direction of the electric field is unchanged. The spectrum of NiPc at $\lambda \geq 600$ nm, on the other hand, was distorted substantially by the doping, as observed in Fig. 9(b).

Figure 9(c) shows the EA spectra of the doped device after aging. For V_{bias} = 0 V, the line shape at $\lambda \leq 570$ nm is close to that of the bulk spectrum of C_{60}, although the sign is opposite to that of the as-prepared device in Fig. 9(b). This indicates that the internal electric field in the C_{60} layer is inverted by the aging. By applying a bias voltage of –0.1 V, the sign of the C_{60} signal, so that the direction of the internal field in the C_{60} layer, was again inverted, as expected. The line shape at $\lambda \geq 600$ nm, on the other hand, became totally different from those of the non-doped and the as-prepared doped devices in Figs. 9(a) and (b). This indicates that the EA spectrum of NiPc is completely transformed to that of NiPc-I_x after aging. Important is that the intensity of the NiPc-I_x signal at $\lambda \geq 600$ nm is unchanged by applying a bias voltage of –0.1 V. This indicates that the observed EA spectrum of NiPc-I_x comes from the interface of the NiPc-I_x layer and the bulk spectrum of NiPc-I_x is too small to be detected. This is as expected, because

NiPc-I_x has an electric conductivity several orders higher than that of C_{60} so that all the built-in potential under V_{bias} = 0 V and all the externally applied electric field exist in the bulk of the C_{60} layer and the interfaces, but not in the bulk of the NiPc-I_x layer.

In Fig. 9(c), finite signal intensity is observed at 840 nm where neither NiPc nor C_{60} shows absorption. This is due to a non-zero base line caused by an instrumental problem. The assumed baselines are drawn in all the EA spectra in Figs. 7-9.

4. Discussion

4.1. Band diagrams

The present experimental results are explained based on the band diagrams shown in Fig. 10. In the non-doped heterojunction device ITO/NiPc/C_{60}/In/Al (Fig. 10(a)), band bending occurs near the NiPc/C_{60} interface. Since the slope of the band is proportional to the internal electric field, there exist electric fields in the NiPc and C_{60} layers near the NiPc/C_{60} interface. These band bending regions correspond to the photocurrent-active regions I and II in Fig. 5 because it has been reported that carrier-generation activity and the internal electric field have a good correlation with each other [24,30,31]. The value of $\Phi_{III}^{(0)}$ in Table I is small but finite even for the non-doped device. This indicates that a small band bending exists in region III, as shown in Fig. 10(a), due to a formation of weak Schottky barrier at the C_{60}/In interface.

The present EA result in Fig. 9(a) indicated that the sign of the average electric field in the bulk of the NiPc layer is opposite to that of the C_{60} layer in the non-doped device. This may indicate a formation of a Schottky barrier at the ITO/NiPc interface as shown in Fig. 10 (a). The corresponding band bending near the ITO/NiPc interface may be larger than that near the NiPc/C_{60} interface, resulting in an opposite sign of the average electric field in the NiPc layer compared to that in the C_{60} layer. The formation of the Schottky barrier at the ITO/NiPc

interface is explained by a relatively low work function of the ITO used in the present study, which is 4.3 eV measured by ultraviolet photoemission spectroscopy. It may be expected that the band bending near the ITO/NiPc interface may cause a carrier generation resulting in a positive photocurrent, especially when illuminated from ITO. However, such a positive photocurrent was not generated as observed in Fig. 4, possibly because the transport of the photogenerated holes from the ITO/NiPc interface to the In/Al electrode may be difficult.

In the doped device ITO/NiPc-I_x/C_{60}/In/Al after sufficient aging (Fig. 10(b)), the internal electric fields in regions I and II near the NiPc-I_x/C_{60} interface almost disappear, but small electric field exists in region III near the C_{60}/In interface, which corresponds to the result $\Phi_I << \Phi_{II}^{(0)} << \Phi_{III}^{(0)}$ in Table I for the doped devices after aging for 55 and 118 days. The direction of the electric field in region III in the doped device is opposite to that in regions I and II in the non-doped device, generating a photocurrent of opposite direction.

In the present doping condition, the doping level x of NiPc-I_x is in the order of unity [20,21], and the doped iodine exists as I_3^- [15,16]. Thus, each NiPc molecule should have ~1/3 hole on the average, and the valence band, or HOMO (highest occupied molecular orbital) band, of NiPc should be ~5/6 filled, as shown in Fig. 10(b). It is difficult to measure the work function of iodine-doped Pc by the usual photoelectron spectroscopy because the measurement by this technique should be made in vacuum so that the doped iodine at the surface of the sample is easily removed. In the present study, the work function of NiPc-I_x was measured in air by using a photoemission-yield spectrometer. The estimated work function of NiPc-I_x was 4.66 eV which is close to a reported work function 4.6 eV of C_{60} [32]. This is why no band bending occurs near the NiPc-I_x/C_{60} interface in Fig. 10(b).

The values of the energy differences between the energy levels in Fig. 10 were estimated as follows. Non-doped Pc film usually has a work function of ~4.8 eV [33]. On the other hand, the

HOMO level of NiPc film on glass in air is 5.05 eV measured on the photoemission-yield spectrometer in the present study. Thus, the energy difference between the Fermi and HOMO levels of the non-doped NiPc in Fig. 10(a) is assumed to be ~0.3 eV. On the other hand, since the width of the HOMO band of Pc film is ~1 eV [34,35] and the HOMO band of NiPc-I_x is 5/6 filled, the difference between the Fermi level and the top of the HOMO band of NiPc-I_x in Fig. 10(b) is ~0.2 eV. The optical absorption spectra in Fig. 2(a) indicates that NiPc and NiPc-I_x have nearly the same HOMO-LUMO (lowest unoccupied molecular orbital) gap of 1.7 eV. On the other hand, reported HOMO, LUMO and Fermi levels of a C_{60} film are 6.2, 3.6 and 4.6 eV [32]. Then, the differences between the LUMO levels of Pc and C_{60} in the doped and non-doped devices are ~0.9 and ~0.4 eV, respectively. Similarly, the difference between the Fermi level and the HOMO level of C_{60} in the doped device is ~1.6 eV, and the difference between the HOMO levels of NiPc and C_{60} in the non-doped device is ~1.3 eV.

In NiPc-I_x, the HOMO band of NiPc is ~5/6 filled, as noted above. In the case of powder NiPc-I_x, it has been suggested that NiPc-I_x shows a metallic transport [20]. However, the NiPc-I_x film in the present device may not be metallic because the doped device ITO/NiPc-I_x/C_{60}/In/Al has a strong rectification property as shown in Fig. 6(b). If NiPc-I_x is metallic, NiPc-I_x works simply as an electrode. In this case, no clear rectification property would be observed by the following reason. If NiPc-I_x is metallic, the device works as a monopolar diode and the barrier height for electron injection to the device would be the energy difference between the Fermi level and the LUMO level of C_{60} both for the forward and reverse bias directions. Since the band bending in the C_{60} layer in Fig. 10(b) is quite small, the barrier height at both sides of the C_{60} layer would be nearly equal (~1.0 eV) and no clear rectification would be observed. Thus, the present NiPc-I_x film works as a *p*-type semiconductor. In other words, the device works as a bipolar diode, and the barrier heights for the electron- and hole-injections under the reverse bias

condition are the energy difference (1.9 eV) between the LUMO level of NiPc-I_x and the Fermi level and the difference (1.6 eV) between the HOMO level of C_{60} and the Fermi level, respectively, which are larger than the barrier heights under the forward bias condition (1.0 and 0 eV, respectively), resulting in a smaller reverse current. The non-metallic nature of the present NiPc-I_x film may be caused by a disorder in the crystal lattice [20].

For the doped device immediately after preparation, the band diagram should be similar to that of non-doped device, because the shapes of the EA spectrum (Fig. 9(b)), the IPCE spectrum (Fig. 3(a)), and the *J-V* curve (Fig. 6(b)) are similar to those of the non-doped device (Figs. 9(a), 4(a), 6(a)). However, the internal electric field of the doped device is much smaller than the non-doped device because the EA signal intensity is much smaller. For the doped device after aging for 33 days, on the other hand, the band diagram should be intermediate between Figs. 10(a) and (b). The slow evolution of the doped device is attributed to a slow establishment of the final energy level alignment at the NiPc-I_x/C_{60} interface: During the sample preparation, some of the iodine at the surface of NiPc-I_x film was removed because the NiPc-I_x film was kept in vacuum during the C_{60} deposition [36]. Thus, the surface of the NiPc-I_x film immediately after device preparation was in a disdoped state. Then, the iodine in the NiPc-I_x film slowly diffused to the Pc/C_{60} interface, and the final energy level alignment was slowly established. This energy level alignment may involve some sort of interface-state formation and a resulting Fermi-level pinning, although details are unknown. It is noted that the duration for the doped device to reach the final stationary state depends on the temperature during the aging. The results shown in Fig. 3 are for a sample prepared in spring. When the sample was prepared in summer, the final stationary state was obtained within 20 days.

In the *J-V* curves of the doped device after aging in Fig. 6(b), the forward current was significantly suppressed at $0 \leq V_{bias} \leq 1$ V. This is explained as follows. Under the forward bias

condition, there exists a barrier for electron transport at the Pc/C_{60} interface which is 0.9 eV in the doped device after aging. On the other hand, the barrier height in the as-prepared device may be close to 0.4 eV because the band diagram should be close to that of the non-doped device (Fig. 10(a)) as discussed above. The larger barrier height in the aged device may be the reason for the smaller current at $0 \leq V_{bias} \leq 1$ V. Effect of the doping on the hole transport, on the other hand, is not clear. The barrier for the hole transport at the Pc/C_{60} interface increases from ~1.3 eV to 1.6 eV by the aging, but the barrier at the ITO/Pc interface decreases from ~0.3 eV to 0 eV, so that the two effects may cancel each other. Although the forward current was suppressed at $0 \leq V_{bias} \leq 1$ V in Fig. 6(b), the doped device ITO/NiPc-I_x/C_{60}/In/Al showed a clear rectification property at $V_{bias} = \pm 2$ V. This is in contrast to the case of the usual Schottky-barrier device of C_{60}, in which clear rectification is observed only when a high work-function metal, such as Pt, is used. A high rectification ratio has been reported for Pt/C_{60}/In/Al [29], but not for Au/C_{60}/In/Al and ITO/C_{60}/In/Al.

In the present simulation of the IPCE spectra, the energy-dependent quantum efficiency of C_{60} defined by Eqs. (6) and (7), which increases for the excitation energy higher than 2.7 eV, gave good fits to the experimental spectra. This result contradicts with the one reported by Peumans et al. for ITO/PEDOT:PSS/Cu-phthalocyanine/C_{60}/BCP/Al heterojunction device in which the experimental spectrum was explained by an energy-independent quantum efficiency both for C_{60} and phthalocyanine [37]. This indicates that the carrier-generation mechanisms of the present samples and those by Peumans et al. are different. The energy-dependent quantum efficiency in the present samples is explained by a domination of the charge separation from the excited states higher than the lowest excited state under high energy excitation [38]. The origin of the difference is unknown at present, but a possible origin might be the difference in the work function of the anode. The present ITO electrode has a work function of 4.3 eV, while the

effective work function in the case of Peumans et al. should be substantially higher because of the insertion of the PEDOT:PSS layer. It is known that the electric field near the Pc/C_{60} interface is significantly affected by the work function of the anode [39]. The different features in the electric field distribution near the donor/acceptor interface may possibly make the carrier-generation mechanism different.

4.2. With Au electrode for C_{60} instead of In/Al

It has been shown in the present study that, in the doped device ITO/NiPc-I_x/C_{60}/In/Al, the internal electric field near the NiPc-I_x/C_{60} interface disappears and the weak Schottky barrier at the C_{60}/In interface controls the photocurrent generation of the device. This result leads us to an expectation that, if a higher work function metal is used as an electrode for C_{60} instead of In/Al, the Schottky barrier at the C_{60}/metal interface becomes higher and the effect of the electric field in region III is more clearly seen in the photocurrent generation. Thus, a doped device ITO/NiPc-I_x/C_{60}/Au shown in Fig. 11, as well as a non-doped device ITO/NiPc/C_{60}/Au, was prepared. Figure 12 shows the IPCE spectra of these non-doped and doped devices. For the non-doped device (Fig. 12(a)), negative photocurrent was observed. This indicates that the electric field in region II is larger than that in region III. For the doped device, on the other hand, positive photocurrent was observed even for the as-prepared device (Fig. 12(b)). This indicates that the electric field in region III is larger than that in region II. The values of Φ_I, $\Phi_{II}^{(0)}$ and $\Phi_{III}^{(0)}$ estimated by the simulation of the IPCE spectra are listed in Table I. In the doped device, Φ_I, $\Phi_{II}^{(0)}$ are negligibly small and the photocurrent generation is controlled by $\Phi_{III}^{(0)}$. These results are as expected and give another evidence that the inversion of the photocurrent direction in the ITO/NiPc-I_x/C_{60}/In/Al device by the aging was really due to an existence of a Schottky

barrier at the C_{60}/In interface. It is noted that the values of Φ_{I}, $\Phi_{II}^{(0)}$ and $\Phi_{III}^{(0)}$ of the non-doped ITO/NiPc/C_{60}/Au are much smaller than those of the non-doped ITO/NiPc/C_{60}/In/Al. This is due to a cancellation between the activities of regions III and II (or I) in the former device.

5. Conclusions

Photocurrent generation in an iodine-doped device ITO/NiPc-I_x/C_{60}/In/Al was studied, in which the C_{60} film effectively encapsulates the doped iodine into the NiPc-I_x layer to prevent the reaction of iodine with In. By keeping the device in air after preparation, the device slowly evolved to a stationary state in which no band bending exists near the NiPc-I_x/C_{60} interface and a weak Schottky barrier at the C_{60}/In interface causes the photocurrent generation of the device. Thus, the iodine doping of NiPc has an effect to quench the electric field and the photocurrent-generation activity near the NiPc/C_{60} junction. This made it possible to detect the weak Schottky barrier at the C_{60}/In interface. The present NiPc-I_x film is non-metallic although the HOMO band is ~5/6 filled. This is probably due to a disorder in the crystal lattice. If one can make the NiPc-I_x film metallic by controlling the crystallinity, the situation will be changed dramatically, which is a subject for the future study.

Acknowledgements

The authors thank Riken Keiki Co., Ltd. for measuring the Fermi level of NiPc-I_x using AC-2.

References

[1] H. Spanggaard, F. C. Krebs, Sol. Energy Mater. Sol. Cells 83 (2004) 125.

[2] M. Pfeiffer, A. Beyer, B. Plönnigs, A. Nollau, T. Fritz, K. Leo, D. Schlettwein, S. Hiller, D. Wöhrle, Sol. Enerby Mater. Sol. Cells 63 (2000) 83.

[3] J. Blochwitz, M. Pfeiffer, T. Fritz, K. Leo, Appl. Phys. Lett. 73 (1998) 729.

[4] X. Zhou, J. Blochwitz, M. Pfeiffer, A. Nollau, T. Fritz, K. Leo, Adv. Funct. Mater. 11 (2001) 310.

[5] C. Uhrich, D. Wynands, S. Olthof, M. K. Riede, K. Leo, S. Sonntag, B. Maennig, M. Pfeiffer, J. Appl. Phys. 104 (2008) 043107.

[6] K. Kudo, M. Iizuka, S. Kuniyoshi, K. Tanaka, Electr. Eng. Jpn. 134 (2001) 10.

[7] M. Iizuka, M. Nakamura, K. Kudo, Jpn. J. Appl. Phys. Part 1, 41 (2002) 2720.

[8] H. Sakuma, M. Iizuka, M. Nakamura, K. Kudo, K. Tanaka, Jpn. J. Appl. Phys. Part 1, 41 (2002) 2727.

[9] S. Horiuchi, T. Hasegawa, Y. Tokura, J. Phys. Soc. Jpn. 75 (2006) 51016.

[10] W. A. Nevin, G. A. Chamberlain, J. Appl. Phys. 69 (1991) 4324.

[11] G.. D. Sharma, S. G. Sangodkar, M. S. Roy, Mater. Sci. Eng. B41 (1996) 222.

[12] A. C. Varghese, C. S. Menon, J. Mater. Sci. 41 (2006) 3521.

[13] M. Kudo, K. Iketaki, T. Kaji, M. Hiramoto, Appl. Phys. Lett. 98 (2011) 073311.

[14] G. Wegner, Angew. Chem. Int. Ed. Engl. 20 (1981) 361.

[15] J. L. Petersen, C. S. Schramm, D. R. Stojakovic, B. M. Hoffman, T. J. Marks, J. Am. Chem. Soc. 99 (1977) 286.

[16] C. J. Schramm, R. P. Scaringe, D. R. Stojakovic, B. M. Hoffman, J. A. Ibers, T. J. Marks, J. Am. Chem. Soc. 102 (1980) 6702.

[17] R. P. Linstead, J. M. Robertson, J. Chem. Soc. (1936) 1736.

[18] J. Janczak, R. Kubiak, J. Alloys Compd. 190 (1992) 121.

[19] A. Hoshino, Y. Takenaka, H. Miyaji, Acta Cryst. B59 (2003) 393.

[20] I. Hiromitsu, N. Ikeda, T. Ito, Synth. Met. 85 (1997) 1737.

[21] I. Hiromitsu, H. Yamamoto, T. Ito, Phys. Rev. B52 (1995) 7252.

[22] I. H. Campbell, T. W. Hagler, D. L. Smith, J. P. Ferraris, Phys. Rev. Lett. 76 (1996) 1900.

[23] P. A. Lane, J. Rostalski, C. Giebeler, S. J. Martin, D. D. C. Bradley, D. Meissner, Sol. Energy Mater. Sol. Cells 63 (2000) 3.

[24] I. Hiromitsu, Y. Murakami, T. Ito, J. Appl. Phys. 94 (2003) 2434.

[25] M. Mizuno, J. Tanaka, I. Harada, J. Phys. Chem. 85 (1981) 1789.

[26] Y. Yoshida, S. Tanaka, Y. Fujita, I. Hiromitsu, J. Appl. Phys. 106 (2009) 064510.

[27] Z. D. Popovic, Chem. Phys. 86 (1984) 311.

[28] S. Kazaoui, R. Ross, N. Minami, Phys. Rev. B52 (1995) R11665.

[29] I. Hiromitsu, R. Shinto, M. Kitano. T. Kitauchi, T. Ito, Jpn. J. Appl. Phys. 41 (2002) 6517.

[30] I. Hiromitsu, G. Kinugawa, Synth. Met. 153 (2005) 73.

[31] I. Hiromitsu, G. Kinugawa, Jpn. J. Appl. Phys. 44 (2005) 60.

[32] N. Hayashi, H. Ishii, Y. Ouchi, K. Seki, J. Appl. Phys. 92 (2002) 3784.

[33] Y. Harima, K. Yamashita, H. Ishii, K. Seki, Thin Solid Films 366 (2000) 237.

[34] S. Tanaka, Y. Yoshida, M. Nonomura, K. Yoshino, I. Hiromitsu, Thin Solid Films 516 (2008) 1006.

[35] S. Tanaka, T. Hanada, K. Ono, K. Watanabe, K. Yoshino, I. Hiromitsu, Appl. Phys. Lett. 97 (2010) 253306.

[36] I. Hiromitsu, H. Aoyama, J. Takeuchi, T. Ito, J. Phys. Soc. Jpn. 60 (1991) 3525.

[37] P. Peumans, A. Yakimov, S. R. Forrest, J. Appl. Phys. 93 (2003) 3693.

[38] C. Im, E. V. Emelianova, H. Bässler, H. Spreitzer, H. Becker, J. Chem. Phys. 117 (2002)

2961.

[39] Y. C. Zhou, Z. T. Liu, J. X. Tang, C. S. Lee, S. T. Lee, J. Electron Spectros. Relat. Phenom. 174 (2009) 35.

Figure and Table captions

Fig. 1. Scheme of ITO/NiPc-I_x/C_{60}/In/Al heterojunction device, and the molecular structure of NiPc and C_{60}. The positive directions of the current and applied bias voltage are defined in the figure.

Fig. 2. Optical absorption spectra. (a) NiPc-I_x films on quartz immediately after preparation and after keeping the film for 9 months in air, and NiPc film on quartz. (b) C_{60} films on quartz before and after treatment with I_2 vapor for 2 days at 30°C. (c) NiPc-I_x /C_{60} films on quartz immediately after preparation and after being kept for 9 months in air, and NiPc/C_{60} film on quartz. The film thicknesses of NiPc and C_{60} are 100 and 54 nm, respectively.

Fig. 3. IPCE spectra of doped device ITO/NiPc-I_x/C_{60}/In/Al. (a) Immediately after the device preparation, and after aging in air for (b) 33 days, (c) 55 days, and (d) 118 days. V_{bias} = 0 V. The solid lines are theoretical ones (see text).

Fig. 4. IPCE spectra of non-doped device ITO/NiPc/C_{60}/In/Al. (a) Immediately after the device preparation, and after aging in air for (b) 55 days, and (c) 118 days. V_{bias} = 0 V. The solid lines are theoretical ones (see text).

Fig. 5. Model for the simulation of IPCE spectra. Three photocurrent-active regions I, II and III exist in the device. The sign of the photocurrent generated is negative for regions I and II and positive for region III.

Fig. 6. Bias dependence of dark current density of (a) non-doped device ITO/NiPc/C_{60}/In/Al,

and (b) doped device ITO/NiPc-I_x/C_{60}/In/Al.

Fig. 7. EA spectra of a non-doped Schottky-junction device ITO/NiPc(150 nm)/In(20 nm)/Al(30 nm) with (a) V_{bias} = 1.5 V, (b) V_{bias} = 0 V and (c) V_{bias} = −1.5 V. The estimated bulk and interface spectra of the non-doped NiPc film, as well as the sum of them, are also shown.

Fig. 8. EA spectra of a Schottky-junction device ITO/C_{60}(100 nm)/In(20 nm)/Al(30 nm) with (a) V_{bias} = 1 V, (b) V_{bias} = 0 V and (c) V_{bias} = −1 V. The estimated bulk and interface spectra of the C_{60} film, as well as the sum of them, are also shown.

Fig. 9. EA spectra of (a) non-doped heterojunction device ITO/NiPc/C_{60}/In/Al after aging for 150 days, and doped device ITO/NiPc-I_x/C_{60}/In/Al (b) immediately after preparation and (c) after aging for 90, or 99 days in air. V_{bias} = 0 V for (a) and (b), and V_{bias} = 0 and −0.1 V for (c). The bulk spectrum of the C_{60} film is also shown in (a), (b) and (c), and the bulk spectrum of the non-doped NiPc film is shown in (a) and (b).

Fig. 10. Proposed energy band diagrams of (a) non-doped device ITO/NiPc/C_{60}/In/Al, and (b) doped device ITO/NiPc-I_x/C_{60}/In/Al in a stationary state after sufficient aging in air.

Fig. 11. Scheme of ITO/NiPc-I_x/C_{60}/Au heterojunction device. The positive direction of the current is defined in the figure.

Fig. 12. IPCE spectra of (a) non-doped device ITO/NiPc/C_{60}/Au immediately after preparation, and doped device ITO/NiPc-I_x/C_{60}/In/Al (b) immediately after preparation and (c) after aging

for 13 days in air. V_{bias} = 0 V. The solid lines are theoretical ones (see text).

Table I. Quantum efficiencies Φ_I, $\Phi_{II}^{(0)}$ and $\Phi_{III}^{(0)}$ for the active regions I, II and III obtained by a simulation of the IPCE spectra in Figs. 3, 4 and 12. The widths of the active regions I, II and III were fixed to 20 nm in the simulation, so that the estimated values of Φ_I, $\Phi_{II}^{(0)}$ and $\Phi_{III}^{(0)}$ are interpreted as the carrier generation activities of the corresponding regions.

Table I

Table I. Quantum efficiencies Φ_I, $\Phi_{II}^{(0)}$ and $\Phi_{III}^{(0)}$ for the active regions I, II and III obtained by a simulation of the IPCE spectra in Figs. 3, 4 and 12. The widths of the active regions I, II and III were fixed to 20 nm in the simulation, so that the estimated values of Φ_I, $\Phi_{II}^{(0)}$ and $\Phi_{III}^{(0)}$ are interpreted as the carrier generation activities of the corresponding regions.

	Φ_I	$\Phi_{II}^{(0)}$	$\Phi_{III}^{(0)}$	IPCE spectrum
ITO/NiPc/C_{60}/In/Al				
As prepared	0.060	0.19	0.035	Fig. 4(a)
After 55 days	0.012	0.082	0.021	Fig. 4(b)
After 118 days	0.0040	0.017	< 0.003	Fig. 4(c)
ITO/NiPc-I_x/C_{60}/In/Al				
As prepared	0.0080	0.13	0.050	Fig. 3(a)
After 33 days	0.0025	0.020	0.031	Fig. 3(b)
After 55 days	0.0010	0.0050	0.026	Fig. 3(c)
After 118 days	0.0010	0.0050	0.026	Fig. 3(d)
ITO/NiPc/C_{60}/Au				
As prepared	0.00050	0.0024	0.00040	Fig. 12(a)
ITO/NiPc-I_x/C_{60}/Au				
As prepared	< 0.00002	< 0.0002	0.0037	Fig. 12(b)
After 13 days	< 0.00001	< 0.00005	0.00085	Fig. 12(c)

Fig.1
Click here to download high resolution image

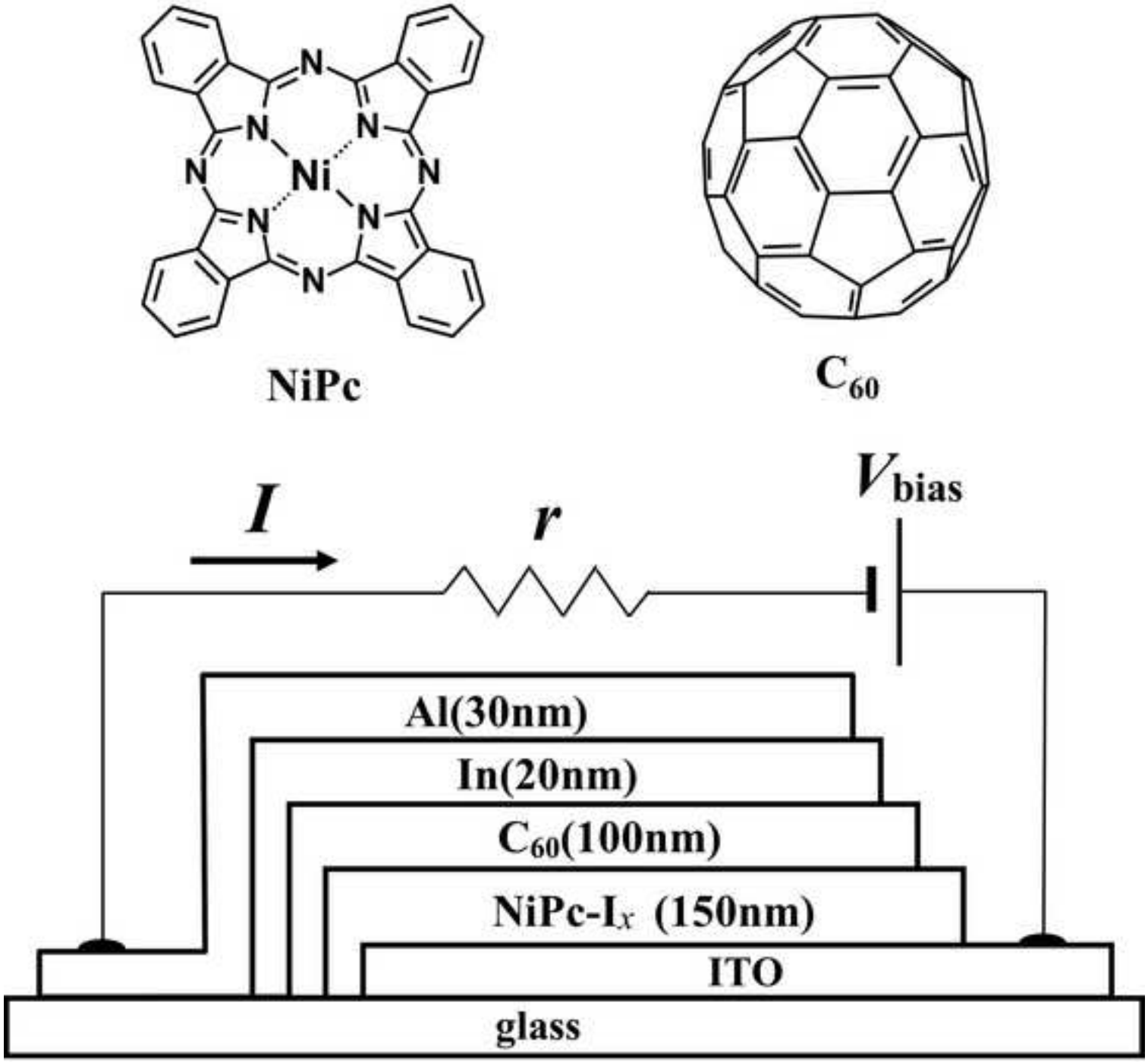

Fig.2
Click here to download high resolution image

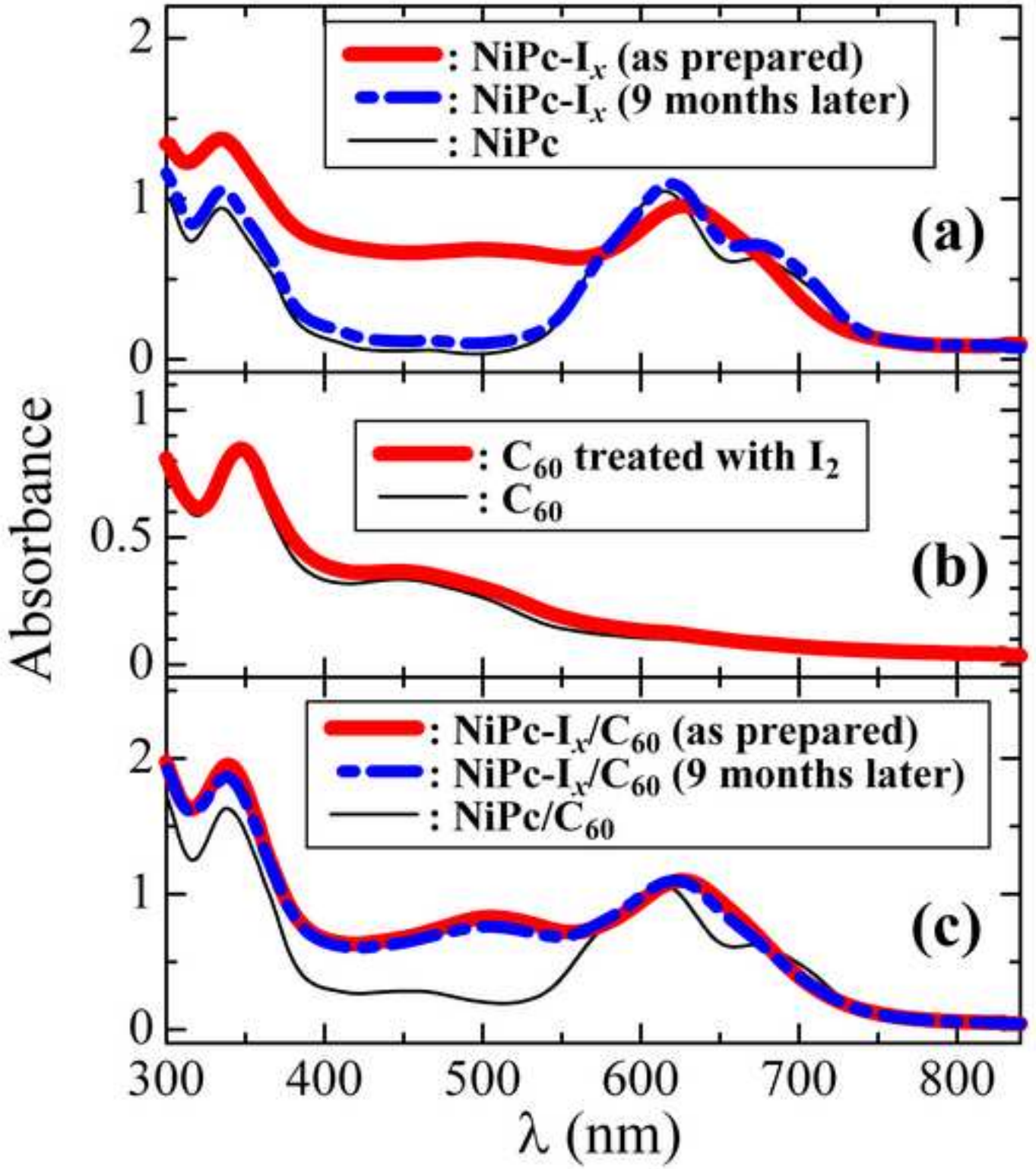

Fig.3

Click here to download high resolution image

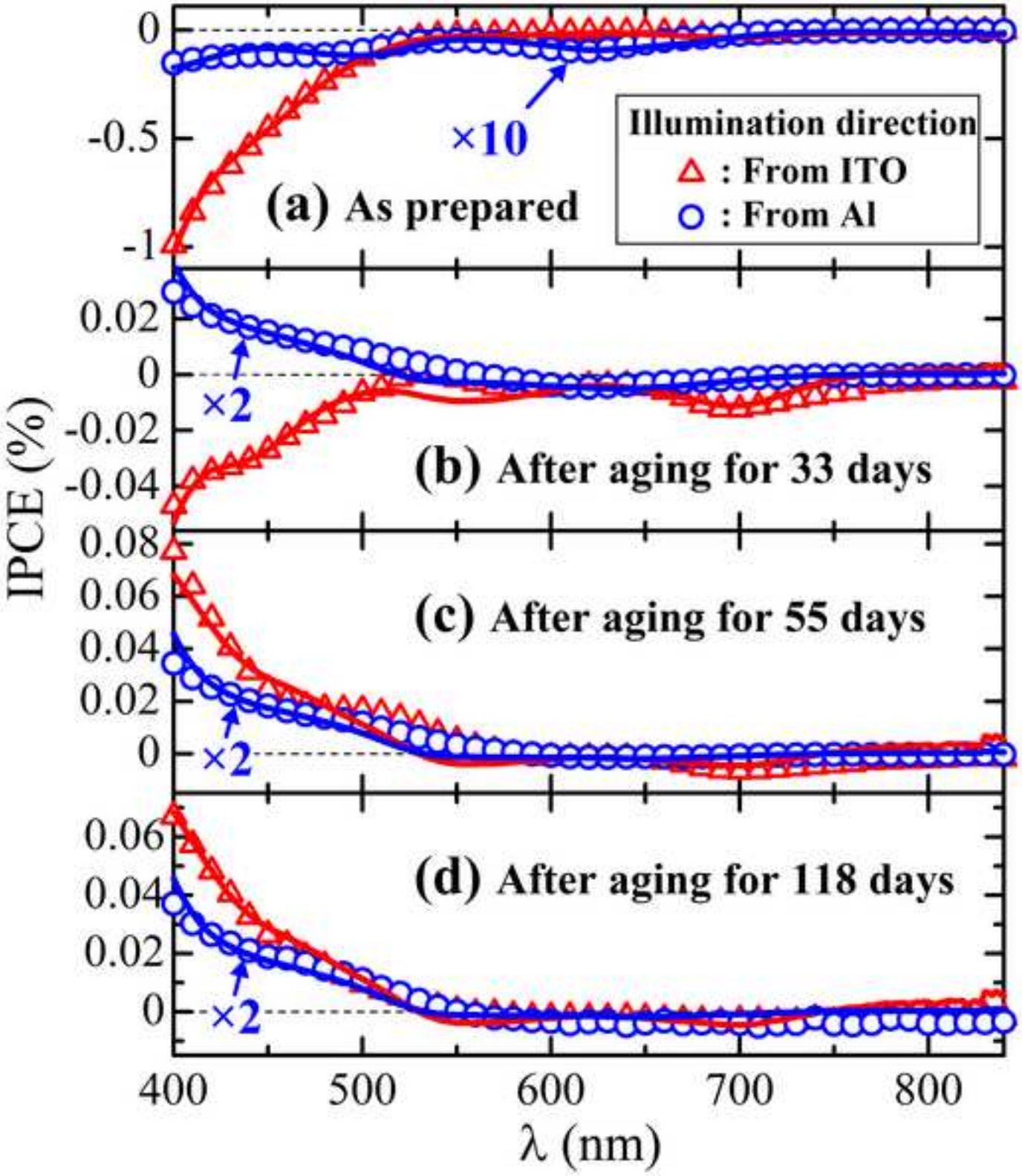

Fig.4

Click here to download high resolution image

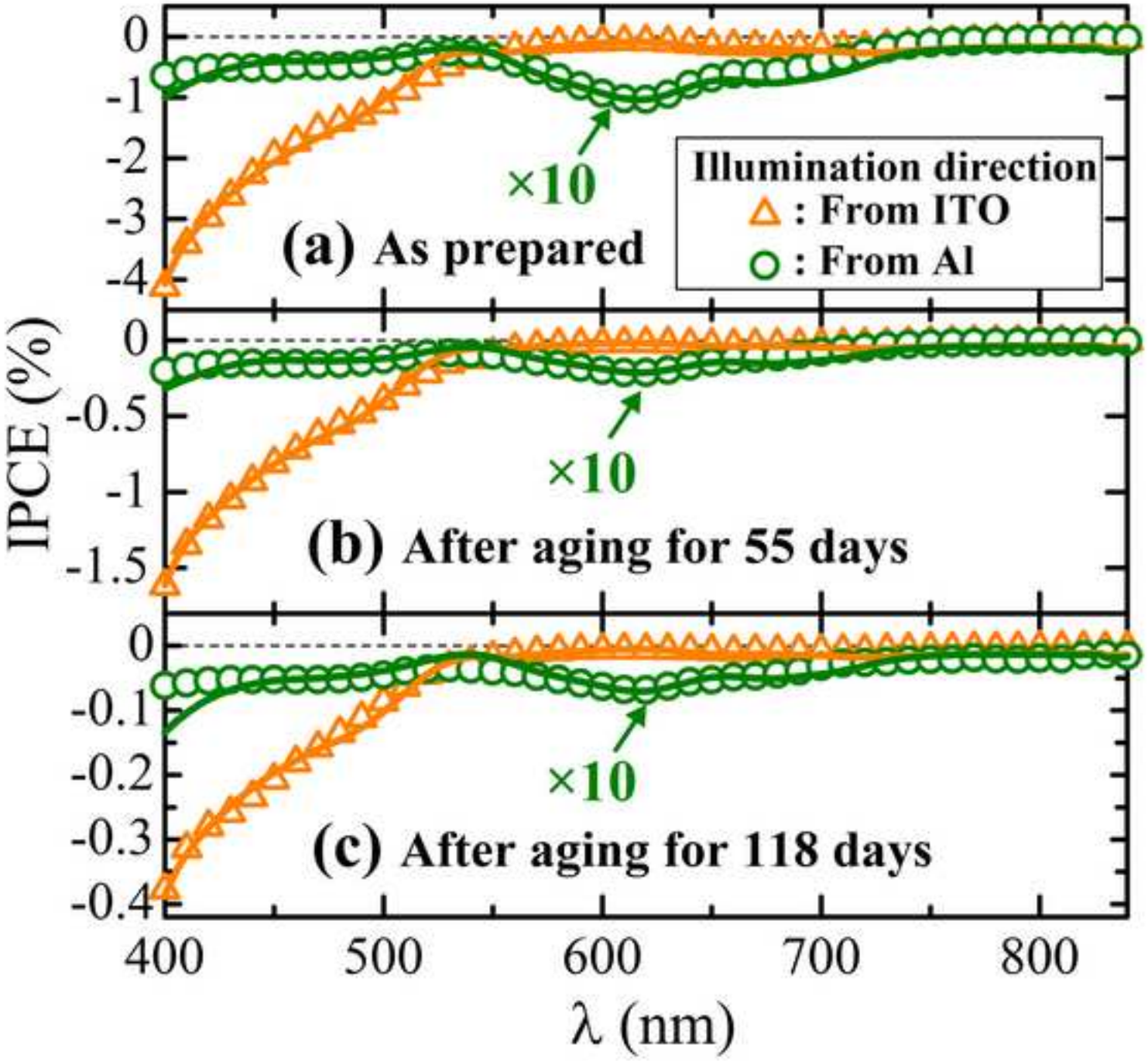

Fig.5

Click here to download high resolution image

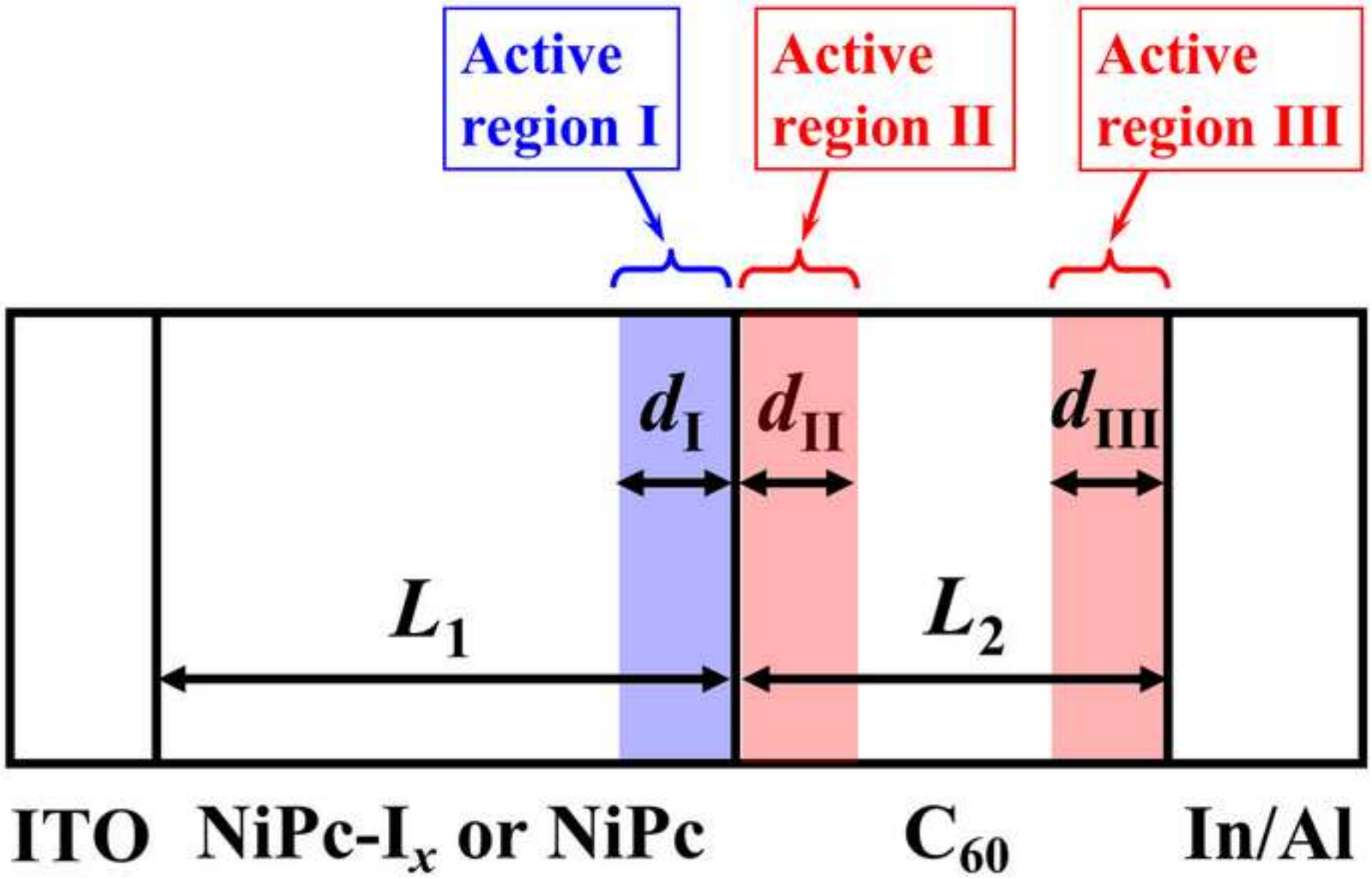

Fig.6

Click here to download high resolution image

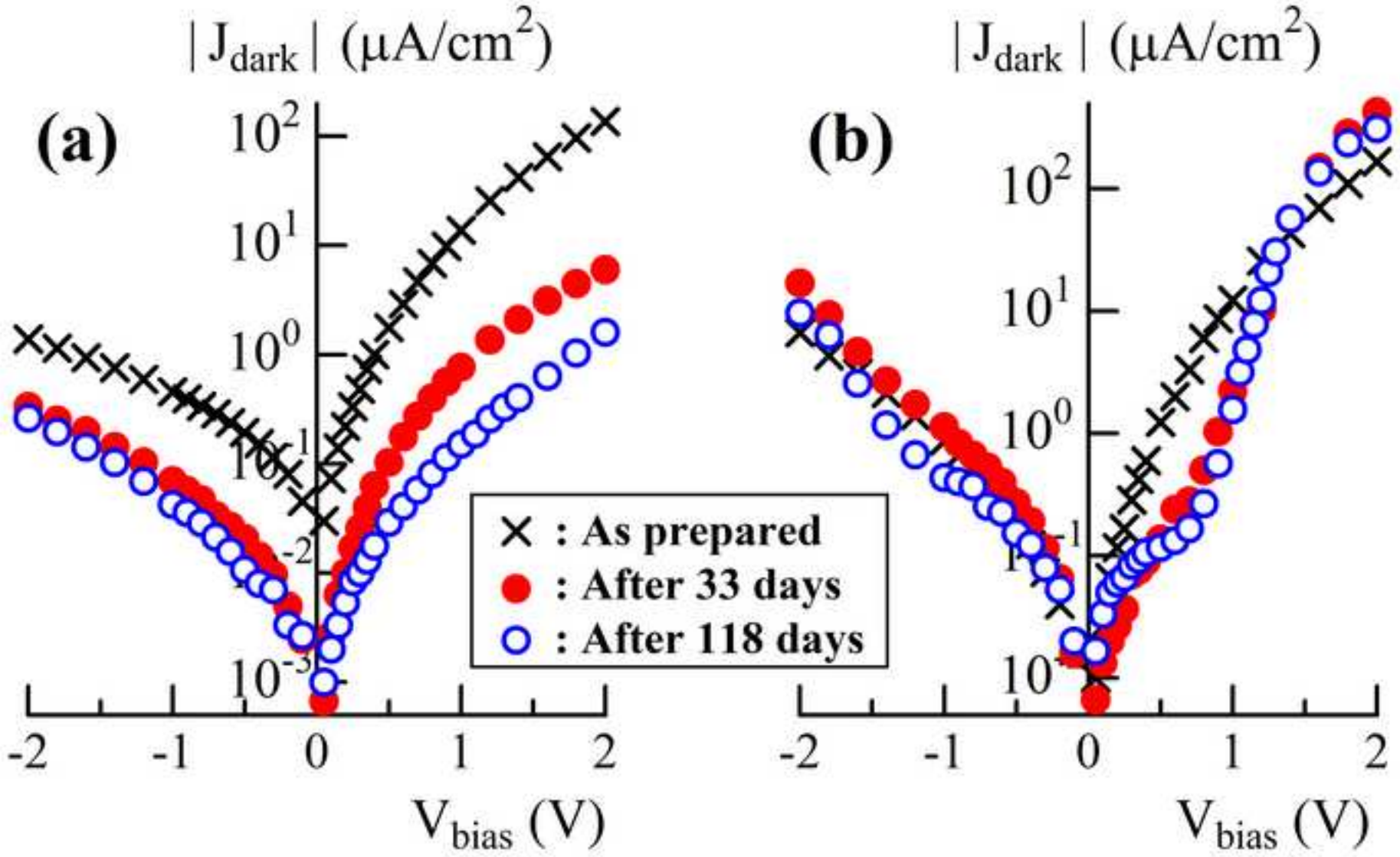

Fig.7

Click here to download high resolution image

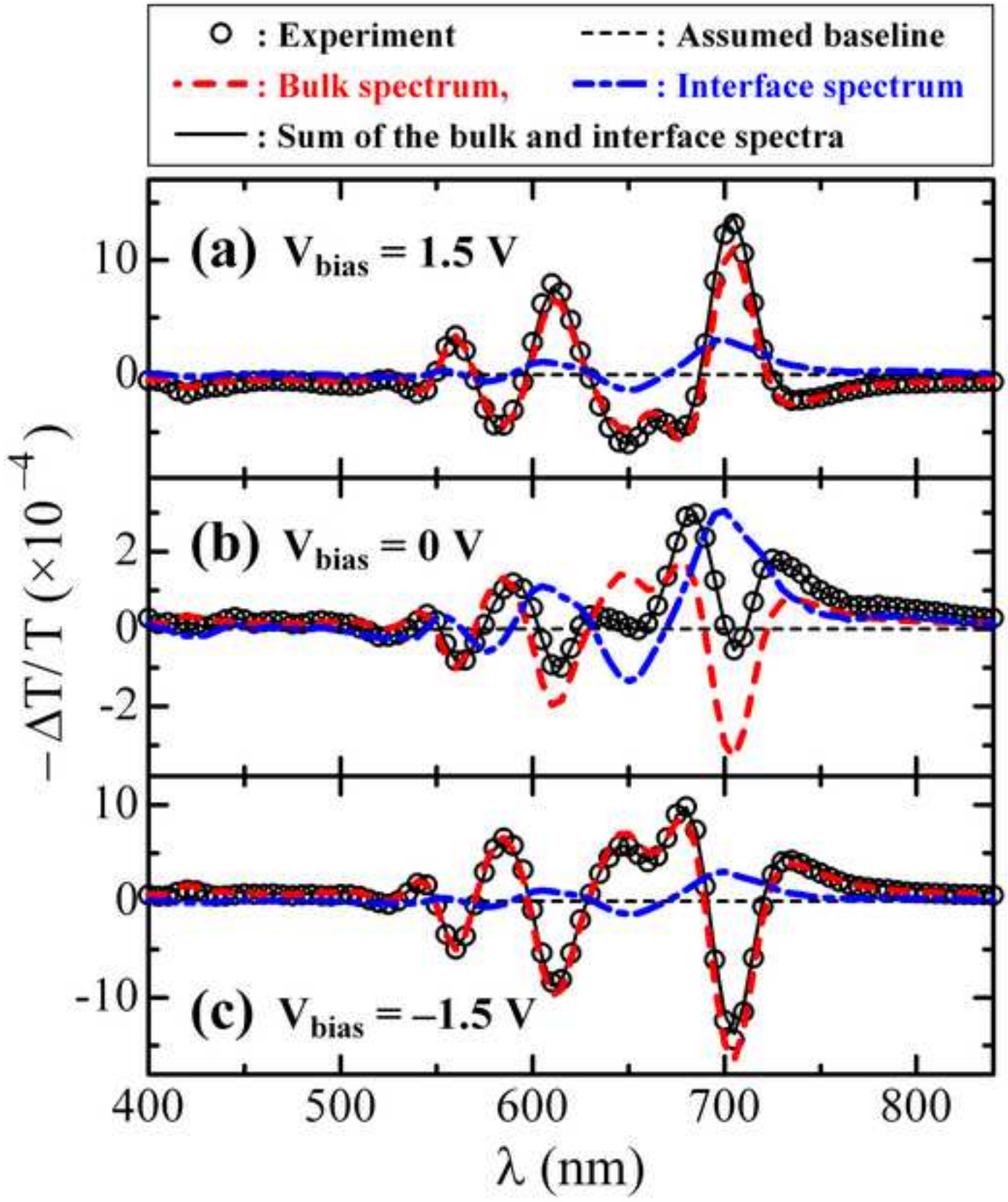

Fig.8
Click here to download high resolution image

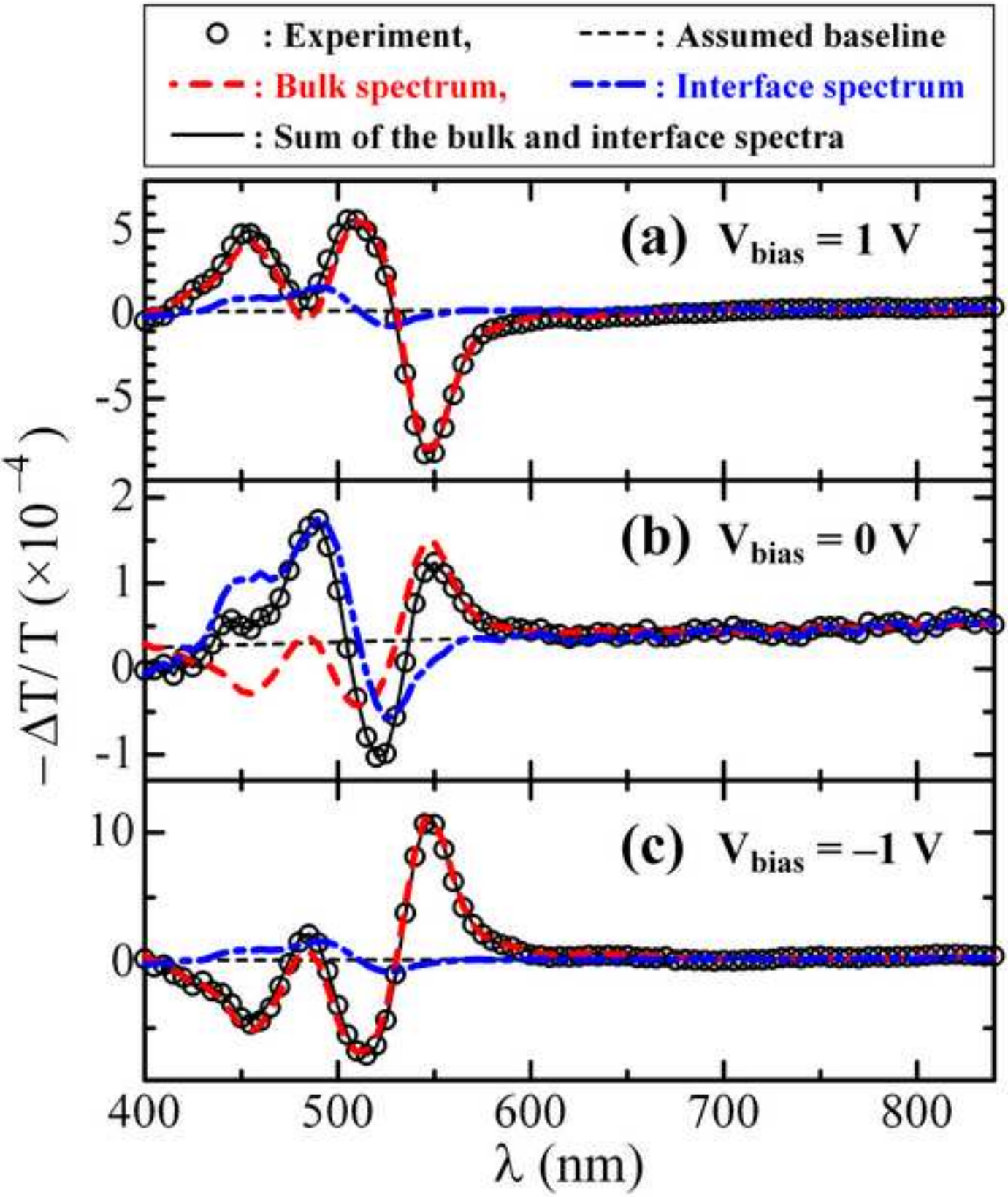

Fig.9

Click here to download high resolution image

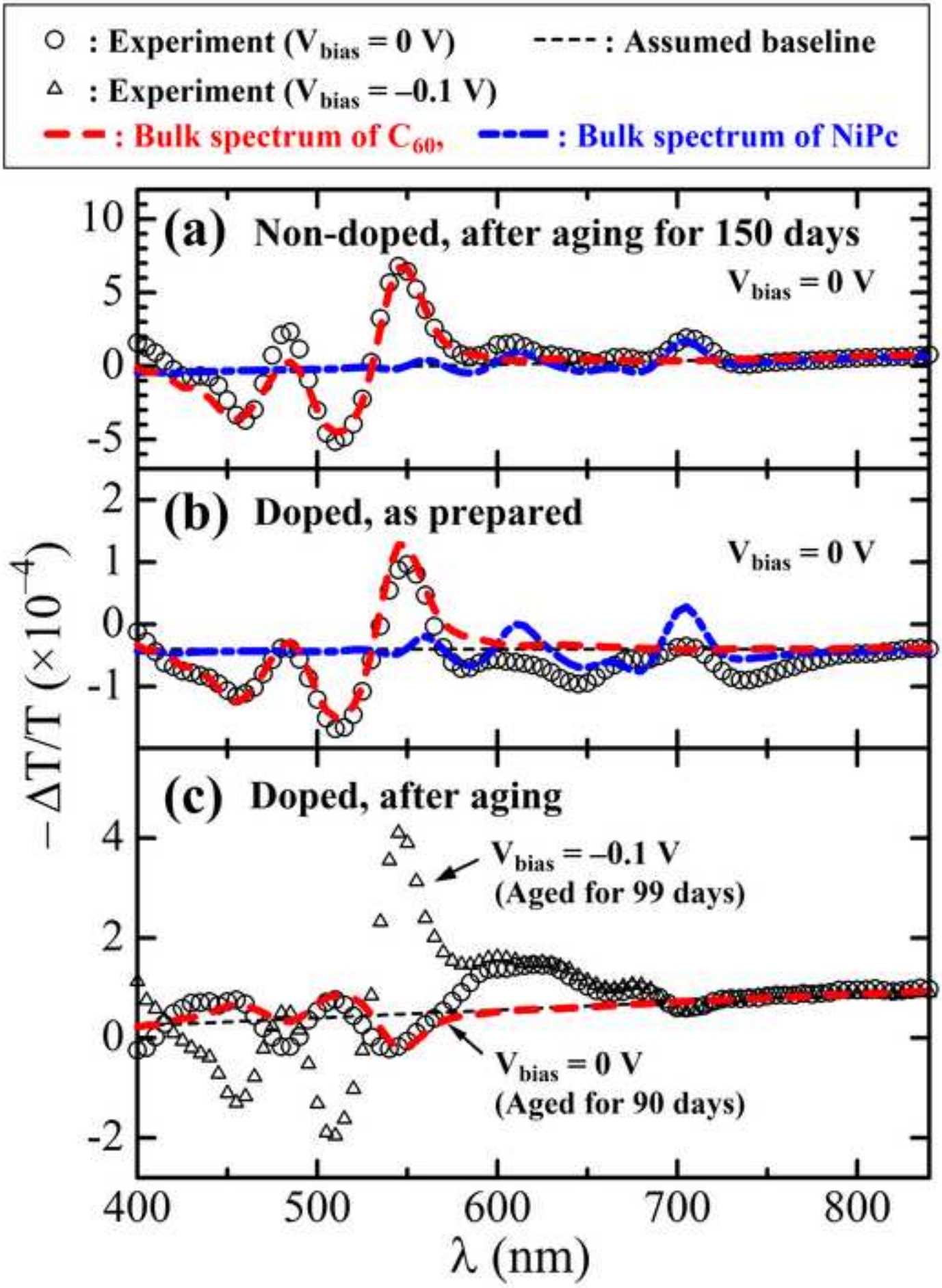

Fig.10
Click here to download high resolution image

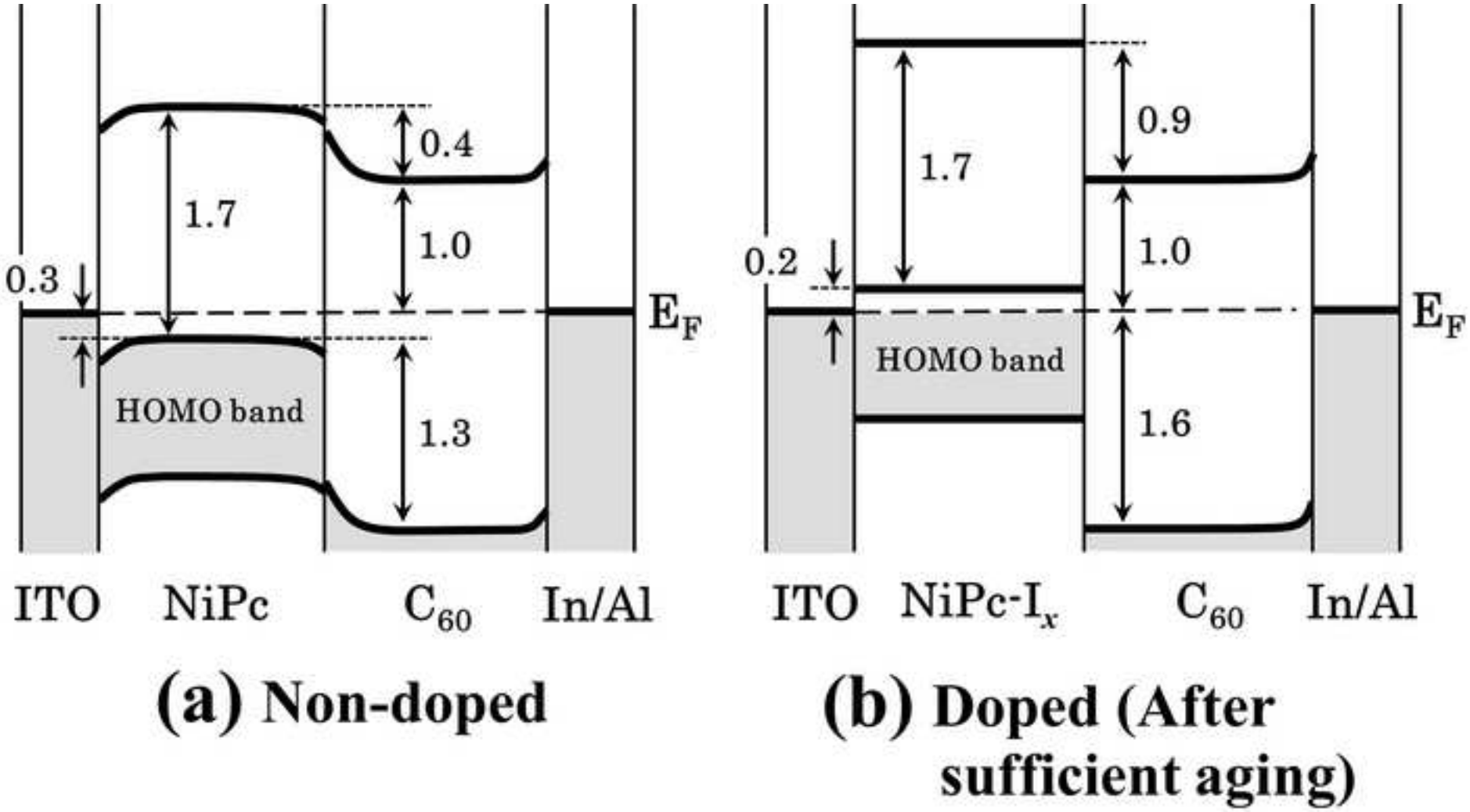

Fig.11

Click here to download high resolution image

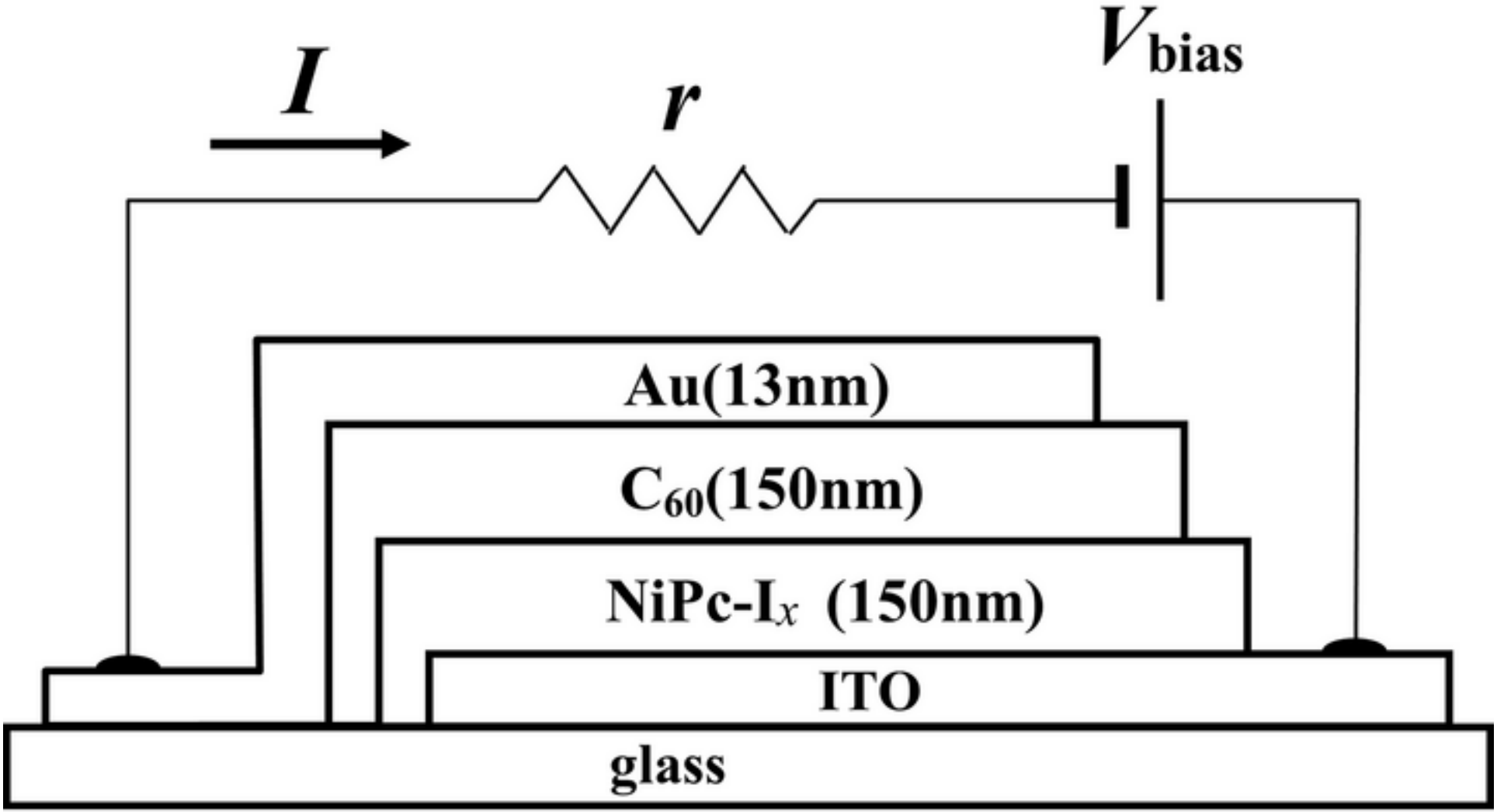

Fig.12

Click here to download high resolution image